

# Chapter 3

## The Millitrap

*This chapter discusses the design, operation, and performance of the mm-scale magnetic trap; portions of this chapter were presented in the publication:*

- *K. L. Moore, T. P. Purdy, K. W. Murch, K. R. Brown, K. Dani, S. Gupta, and D. M. Stamper-Kurn, "Bose-Einstein condensation in a mm-scale Ioffe-Pritchard trap," Applied Physics B **82**, 533-538 (2006). Included in Appendix F.*

As discussed in chapters 1 and 2, the main design criterion for the magnetic trapping system is the integration with a high-finesse optical cavity. In the 2002 review article "Cavity QED - Coherence in Context," the authors discuss a number of high-finesse optical cavity systems with the potential to access the strong atom-photon coupling regime [72]. However, at that time, only one cavity implementation had successfully proven its worth for optical cavity QED with laser-cooled atoms<sup>1</sup>— namely, the optical Fabry-Perot cavities developed by Jeff Kimble *et al.* and manufactured by Research Electro-Optics (REO) [73]. These cavities are formed by  $\sim 3$  mm outer diameter (OD) glass substrates which have been coned down to a 1 mm concave surface, superpolished, and coated with a numerous alternating layers of high-index ( $\text{Ta}_2\text{O}_5$ ,  $n_H = 2.04$ ) and low-index ( $\text{SiO}_2$ ,  $n_L = 1.46$ ) dielectric material [74]. The mirror separation of the substrates could vary from 10's to 100's of microns depending on the desired implementation, but the size scale of interest

---

<sup>1</sup>The pioneering experiments of Haroche *et al.* [37] with Rydberg atoms and *microwave* cavities should be mentioned here as an excellent cavity QED implementation, but an inappropriate one for a magnetically-trapped atoms.

for the design of the magnetic trapping system that will deliver the cold atoms into the cavity was the OD of the mirrors. The basic structure of the REO mirrors used in this work is presented in Figure 3.1.

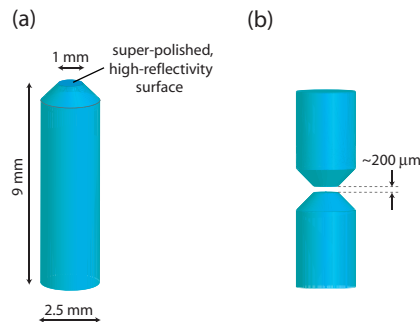


Figure 3.1: The high-finesse optical cavity mirrors. (a) A single mirror, with the critical dimensions listed. The outer diameter is approximately 2.5 mm, and the super-polished, dielectric-coated face is coned down to 1 mm. (b) Two mirrors facing each other form a Fabry-Perot cavity. The optical properties of the mirrors are presented in chapter 6.

The optical properties of the cavity will be discussed in chapter 6, but for the purposes of this chapter we are concerned with the dimensions of the mirrors which will dictate the design of the magnetic trap. Engineers at REO claimed that significantly narrowing the OD from the 3 mm used by the Kimble group was not possible with the current manufacturing capabilities of their plant, but they felt comfortable going as low as 2.5 mm. The second nonstandard request we made was for a relatively long substrate, finally settling on 9 mm, twice the normal length<sup>2</sup>. The substrates built by REO were ultimately two 4.5 mm long substrates epoxied together<sup>3</sup>. With the crucial dimensions of the cavity being the 2.5 mm OD and the 9 mm substrate length, the *millimeter* became the natural length scale for the engineering task that was required. The magnetic trap which resulted from this thinking also had characteristic dimensions expressed in millimeters, and the verbal contraction of the length scale and intended function became both the name of the device and the title

<sup>2</sup>The extra length was required because the millitrap assembly eventually occupied the front 4 mm of the substrate, and the cavity length and mounting structure were pushed back substantially (see chapter 6).

<sup>3</sup>This does not compromise the cavity properties because any reflection/scattering only occurs on, at most a single pass. Scattering losses on the mirror face, while presumably much smaller than the losses at this interface, are compounded like the finesse,  $\mathcal{F} = 580,000$  in our case.

of this chapter.

### 3.1 Design Considerations

The design began with the following initial criteria:

1. Maintain mechanical decoupling from cavity
2. Accommodate 2.5 mm mirror OD and support structure
3. Match long axis (and if possible, magnetic bias field) of trap with the cavity axis
4. Obtain the largest possible magnetic field curvatures so that an ultracold cloud will be smaller than the mirror separation

The third consideration led us to consider an Ioffe-Pritchard (IP) trap [69], which generates the following field profile

$$\mathbf{B}(\rho, z) = \left[ B_o + \frac{B_z''}{2} \left( z^2 - \frac{\rho^2}{2} \right) \right] \hat{z} + \left( B_\rho' - \frac{B_z''}{2} z \right) \rho \hat{\rho}, \quad (3.1)$$

where  $\rho = \sqrt{x^2 + y^2}$ , and the axial curvature ( $B_z'' = d^2 B_z / dz^2$ ) and transverse gradient ( $B_\rho' = dB_\rho / d\rho$ ) are tunable trap parameters<sup>4</sup>. To lowest order about the origin, the field magnitude is given by

$$B(\rho, z) = B_o + \frac{1}{2} B_z'' z^2 + \frac{1}{2} \left( \frac{B_\rho'^2}{B_o} - \frac{B_z''}{2} \right) \rho^2 \quad (3.2)$$

A particle with magnetic moment  $\mu$  will thus experience a harmonic trap with frequencies

$$\omega_\rho = \sqrt{\mu \left( \frac{B_\rho'^2}{B_o} - \frac{B_z''}{2} \right)} / m \quad (3.3)$$

$$\omega_z = \sqrt{\mu B_z'' / m}. \quad (3.4)$$

Typically, it is easier to obtain a strong transverse trapping frequency  $\omega_\rho$  (by application of a strong transverse gradient  $B_\rho'$  and/or reduction of  $B_o$ ) than it is to obtain a strong axial frequency  $\omega_z$ . With the exception of those produced by atom chips [75, 76, 77], IP magnetic

<sup>4</sup>By “tunable” we mean natural magnetic fields produced by the currents in the electromagnets of the trap.

traps formed by hand-wound current carrying wires only achieve axial field curvatures of  $B_z'' \sim 100 \text{ G/cm}$  [69] due to space constraints from accommodating large MOT beams and/or resistive heating-limited current densities. As this axial curvature yields a trapping frequency of  $\sim 2\pi \times 10 \text{ Hz}$ , we can expect a  $1 \mu\text{K}$  cloud of  $|F = 1, m_F = -1\rangle$   $^{87}\text{Rb}$  atoms to have a size of roughly  $\sim 100 \mu\text{m}$ .

The comparison of this size to typical strongly-coupled optical cavity lengths ( $50 - 200 \mu\text{m}$ ) shows this field curvature to be inadequate by running afoul of the fourth stated criterion. Atom chips can produce IP field profiles with axial curvatures in excess of  $10^6 \text{ G/cm}^2$ , but only in the close proximity ( $\sim 100 \mu\text{m}$ ) of the surface (violating the second criterion). Miniaturizing the current-carrying wires is a very effective method of increasing the field curvature. This is evident by considering that the magnetic field curvature from an electromagnet scales as  $I/d^3$ , where  $I$  is the total current in the wire(s) and  $d$  is the characteristic length scale of the system<sup>5</sup>.

More precisely, the desired field is produced by two coaxial loops (of radius  $R$ , carrying current  $I$ ) in the Helmholtz configuration, separated by a distance  $2d$ . At the trap center (located halfway between the two coils) the axial magnetic field is given by

$$B_z(z) = \left( 2\mu_o I \frac{R^2}{(R^2 + d^2)^{3/2}} \right) + \frac{1}{2} \left( 6\mu_o I \frac{R^2(4d^2 - R^2)}{(R^2 + d^2)^{7/2}} \right) z^2 + O(z^4) \quad (3.5)$$

$$= B_o + \frac{1}{2} \left( 3B_o \frac{4d^2 - R^2}{(R^2 + d^2)^2} \right) z^2 \quad (3.6)$$

$$= B_o + \frac{1}{2} B_z'' z^2. \quad (3.7)$$

A [d,R] contour plot of  $B_z''$  (Figure 3.2(a)) shows the impressive gains promised by miniaturization, where electromagnets constructed on the mm-scale of the cavity mirrors yield field curvature/current ratios of  $10^2 \text{ G/cm}^2/\text{A}$ , as compared to the  $\approx 1 \text{ G/cm}^2/\text{A}$  provided by inch-scale traps.

With the goal of  $100\times$  improvement in curvature and a corresponding factor of  $1/10$  reduction in cloud size, an arrangement of current-carrying wires is sought which achieves a benchmark of  $B_z'' = 10^4 \text{ G/cm}^2$ . Again consulting Figure 3.2, we find that  $\sim 100 \text{ Amps}$

<sup>5</sup>When developing this design in 2002, we considered employing atom chips for this work but came to the conclusion that adding this extra layer of complexity added too many unknowns to this first generation implementation. Tom Purdy, an alumnus of this experiment, is now leading exactly such a second generation project with multiple(!) high-finesse cavities on a microchip.

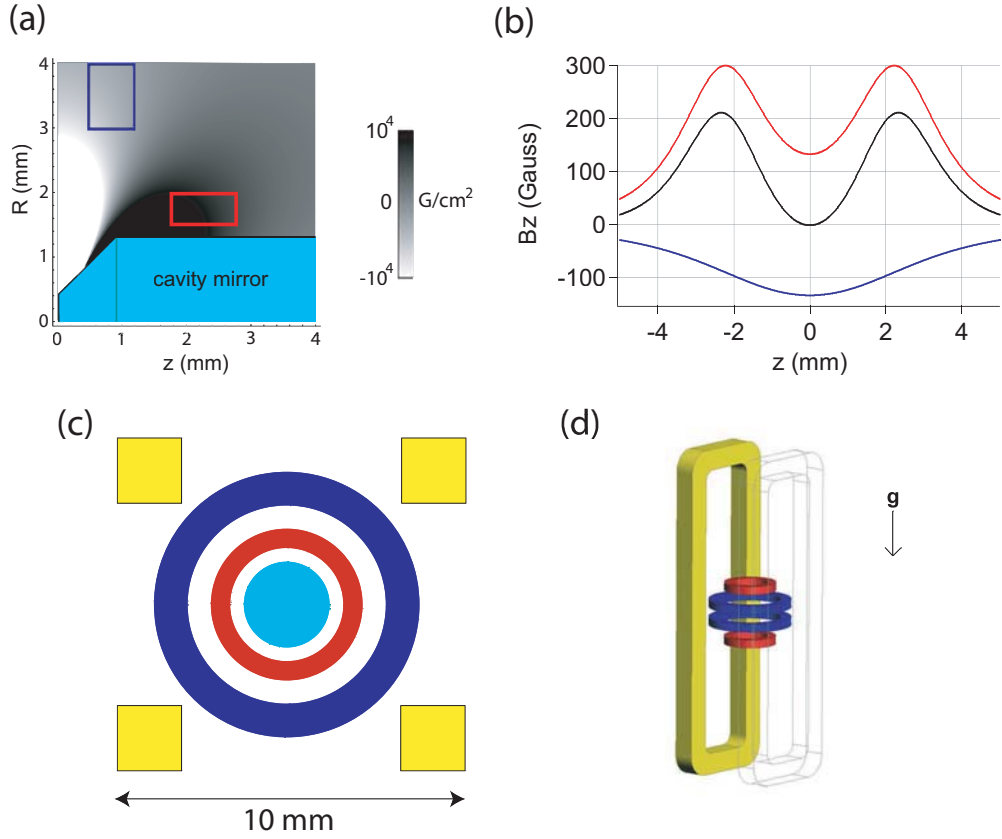


Figure 3.2: Considerations for the placement of the curvature and anti-bias coils. (a) A cavity mirrors (OD = 2.5 mm) is overlaid on a contour plot of  $B_z''$  induced at the origin of the graph if a 10 Amp loop of current is placed at an axial distance  $z$  and a radius  $R$ . The final placement of the 5-turn curvature coils and 4-turn anti-bias coils are shown with their boundaries, represented by red and blue, respectively. (b) Axial field plots for the curvature and anti-bias coils each running 10 Amps of current, with the additive nature of the anti-bias curvature evident from the combined field (black). (c) On-axis view of the cavity/millitrap system. Shown in yellow are the gradient bars, which provide the transverse gradient  $B_\rho'$ . (d) Another view of the millitrap, with gravity oriented properly. For clarity the cavity has been omitted and the nearest gradient coil is shown as transparent.

need to be delivered to a cross-section of  $< 1 \text{ mm}^2$ . Delivering such high current densities is a formidable technical challenge. Employing multiple turns of wire can reduce the problem of delivering large currents into a vacuum chamber, but then electrical insulation between the wires must be used. With or without the use of electrical insulation, resistive heating is of paramount concern. Room temperature copper has a resistivity of  $16.8 \text{ n}\Omega \cdot \text{m}$  [78], so envisioning a  $R = 2 \text{ mm}$  loop of room temperature copper with a cross section of  $0.5 \text{ mm}^2$  gives a resistance of  $4.2 \times 10^{-4} \text{ Ohms}$ . Delivering  $100 \text{ A}$  of total current to this loop will thus generate  $4.2 \text{ W}$  in the loop alone. This is a very significant amount of power to dissipate, especially in the presence of electrical insulation between multiple turns and the close proximity to a highly-sensitive high-finesse cavity!

Altogether, the considerations in the section resulted in the design presented in Figure 3.2, which shows the coils in context with the  $2.5 \text{ mm}$  OD cavity. The curvature coils are situated to maximize curvature while still leaving  $0.25 \text{ mm}$  clearance to the  $2.5 \text{ mm}$  OD cavity mirrors. The anti-bias coils, which run current in the opposite direction as the curvature coils, are placed to control not only the overall bias field at the origin but also to contribute curvature. As depicted, the curvature coils and anti-bias coils will contribute  $100 \text{ G/cm}^2/\text{A}$  and  $33 \text{ G/cm}^2/\text{A}$ . The axial field profiles of these coils are given in Figure 3.2(b). Finally, the “gradient” bars (so named because they produce  $B'_\rho$ ) are packed in with  $4 \text{ mm}^2$  cross-section, and provide a gradient of  $2.5 \text{ G/cm/A}$ .

## 3.2 The Millitrap

As touched on in the preceding section, delivering the necessary current densities presents a significant engineering challenge. In addition to satisfying the design criteria already outlined, the system must also conform to the following technical criteria:

- A. Accommodate at least  $100 \text{ A/mm}^2$  of total current density
- B. Limit delivery current to  $< 20 \text{ A}$
- C. Electrically insulate coils from themselves, each other, and the mounting system
- D. Minimize and dissipate resistive heating such that the temperature of the trap does

not change significantly during operation

The second criterion is due to the difficulty in accommodating large ( $< 20$  A) currents in an ultra-high vacuum system, as well as the desire to use smaller power supplies. Satisfying **A** and **B** clearly necessitates multiple turns of wire per coil, and thus the challenge becomes the general satisfaction of criteria **C** and **D**.

Copper is, of course, the most commonly employed electrical conductor, yet initial attempts using copper wire failed due to overheating issues. This was invariably caused by the fact that typical electrical insulating materials (e.g. Kapton<sup>®</sup> polyimide film) are also thermally insulating, thereby making it very difficult to satisfy criterion **D**.

Ultimately, the best solution proved to be the utilization of aluminum as the current carrier. The primary virtue of aluminum for this application is its ability to be *anodized* (a process described in the next section), by which a microns-thick layer of aluminum-oxide ( $\text{Al}_2\text{O}_3$ ) is grown on the surface. This electrically insulating layer is not a thermal insulating, primarily due to its relatively high thermal conductivity ( $\sim 100\times$  that of Kapton<sup>®</sup>) and small thickness. Anodized aluminum films thus provide a nearly ideal conductor to wrap multiple times into a small cross section, with electrical insulation between layers and nearly all of the area filled with conducting material.

The resistivity of room temperature aluminum is  $26.5 \text{ n}\Omega\cdot\text{m}$ , generating an unacceptable 6.6 Watts of steady-state power for the desired 100 A total current. This problem is ameliorated by operating the system at a lower temperature. Aluminum at liquid nitrogen temperatures has a resistivity of just  $2.5 \text{ n}\Omega\cdot\text{m}$  [79], potentially offering a factor of ten reduction in power generation. Utilizing the latent heat of vaporization of liquid nitrogen is also advantageous to efficiently dissipate the residual Joule heating.

It is important to note that cryogenic operation of the system is no panacea. The millitrap system ultimately required 200 liters of liquid nitrogen for every 8 – 10 hours of operation, and the temperature cycling caused many headaches and aborted data runs, especially after the integration and operation of the high-finesse optical cavity, described in chapter 6.

### 3.2.1 Curvature and Anti-bias Coil Construction

Manufacturing the aluminum coils and adequately dealing with the heating issues proved a very time-consuming, low-yield process, most strongly limited by the fragility of the thin aluminium foil which makes up the coils. There were four major stages of construction, each with their own approximate success-to-failure ratio: anodizing and cleaning (1:2), mandrel-winding and silver epoxying (1:3), baking and mandrel-removal (1:3), installation into mount (1:20). Each stage will be discussed herein, but the main point is that the “hand-wound” construction of the primary current-carrying wires was a tenuous, fragile process in which each aluminum strip had a very remote chance of survival.

Not even included in this dismal mortality spectrum is the initial cutting of the coil, accomplished with a precision shear (courtesy of the UC Berkeley Physics Machine Shop). The coils were cut into a “zig-zag” shape, such as the representation of a curvature coil in Figure 3.3. It was important to “deburr” the strip edges after being cut on the shear, as residual jagged edges were often the cause of electrical shorts after the strip was wound upon itself. Polishing the strips with fine 1500 grit sandpaper and machine oil before anodizing greatly diminished the chances of electrical problems down the line.



Figure 3.3: A curvature coil strip.

The next stage involved anodizing this aluminum strip, a process also carried out in the Physics Machine Shop. Anodizing such flimsy items in the industrial anodizing tank made for an incongruous sight relative to the large pieces the shop usually dealt with, but after some trial and error a “high” yield procedure was developed. To begin, the cut strips were first rinsed in deionized water and then held in a 15% nitric acid bath for approximately a minute. The strips were then suspended in the diluted 15%  $\text{H}_2\text{SO}_4$  bath and the electrochemical anodization process commenced. The system was run at  $\sim 20$  Volts

for only 30 minutes, just half of the typical anodization time for industrial parts. This shortened part of the procedure was a balance between the need for a sufficiently thick layer of the  $\text{Al}_2\text{O}_3$  ceramic surface and the increasingly brittle nature of the same. We found that wires which underwent the entire hour of oxide growth had a much higher chance of breaking during the anodizing or winding process. In contrast, wires anodized for less than 25 minutes were far more likely to have electrical shorts upon winding. Thus, the balance was struck at 30 minutes. After removal from the acid bath, the anodization layer was sealed with a ten minute bath in a warm nickel acetate solution (0.5% nickel acetate, 0.5% boric acid), and then rinsed again in deionized water. The anodized wire was electrically tested with a simple voltmeter acting in resistance mode. The sharp probe ends were touched along the surface, and if the coil did not exhibit “infinite” resistance everywhere along its surface, it was discarded. The  $\approx 50\%$  yield for this process came primarily from coils periodically breaking during the oxide growth stage or the subsequent cleaning/handling process<sup>6</sup>.

After the anodizing process, the strip must be wound upon itself. To cohere the multi-turn coil, an adhesive agent is required. EPO-TEK manufactures a silver-based epoxy (H20E) which is acceptable for UHV conditions, and has the added benefit of being thermally conductive. We were initially concerned about the edge shorts being electrically connected by the epoxy, but we never observed any significant shorting between layers by this alone. The coils were wound upon Teflon<sup>®</sup> mandrels, which were constructed on a lathe to match the desired dimensions of the resultant coil. The use of Teflon<sup>®</sup> proved an absolute necessity, as it was the only common construction material to which the silver epoxy did not adhere. The anodization and Teflon<sup>®</sup> mandrel coil winding is depicted in Figure 3.4.

After removal from the mandrel the bent current lead, which is now on the interior winding, is wrapped over the assembly so that the input and output current leads run parallel from the exterior winding, depicted in Figure 3.5.

As mentioned previously, the probability of survival for the mandrel winding/removal

---

<sup>6</sup>This process followed the standard cleaning procedure for parts which would be introduced to the UHV chamber: a brief bath in the ultrasonic cleaner with deionized water and Simple Green<sup>®</sup>, then deionized water alone, then acetone, and finally methanol.

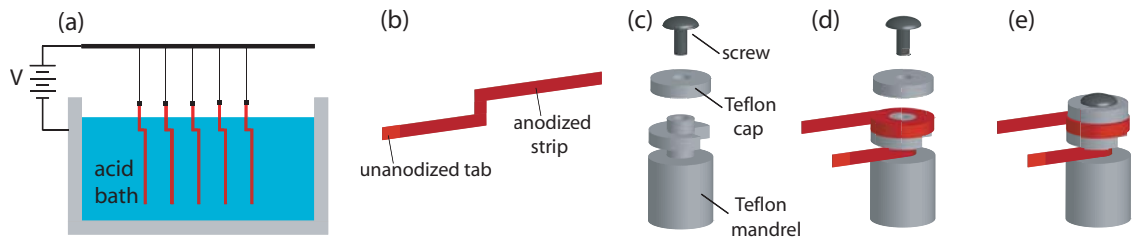


Figure 3.4: Curvature coil construction. (a) As described in text, the aluminum strips are anodized in a sulfuric acid bath, leaving a small tab of unanodized aluminum material which made electrical contact with the strip. (b) After anodization, the function of the “zig-zag” shape is evident when it must be wound around (c) the Teflon<sup>®</sup> mandrel. The mandrel is cut with a notch into which the wire corners are inserted. (d) The long anodized end of the wire is then wound about the spindle of the mandrel, interspersing silver epoxy throughout and in-between each layer. (e) After winding, the tension in the coil is maintained by taping the leads to the mandrel assembly (not shown), and the mandrel assembly is held together by the Teflon<sup>®</sup> cap and the steel screw. The entire mandrel-coil assembly is then baked on a hot plate at 150°C for an hour, setting the epoxy. As the epoxy does not adhere to the Teflon<sup>®</sup>, the intact coil can then be removed and the mandrel is reused for the next coil winding.

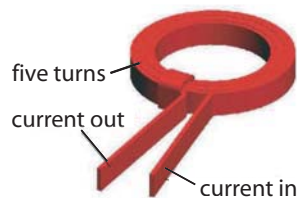


Figure 3.5: A wound curvature coil, with current in/out leads.

stage of the process was approximately 1/3 apiece, with the main mortality vector in both cases being the stress upon the zig-zag portions of the coil which are under heavy tension. Tears at the corner were especially common, and if the coils did not appear perfect upon inspection under a bright-field microscope, they were discarded. Figure 3.6 shows a sample of curvature and anti-bias coils which did not survive the process.

The final and most crucial stage was the insertion of the coils into the mounting structure. The mount itself was a significant engineering challenge, and the construction diagrams for the crucial pieces for this structure are presented in Appendix D. The first,



Figure 3.6: A mass grave of millitrap coils which did not survive the construction process. A U.S. quarter is included for size reference.

and perhaps most critical, mounting piece is the “faceplate” which houses the curvature and anti-bias coils. A diagram of the faceplate (with curvature coils and anti-bias coils incorporated) is presented in Figure 3.7.

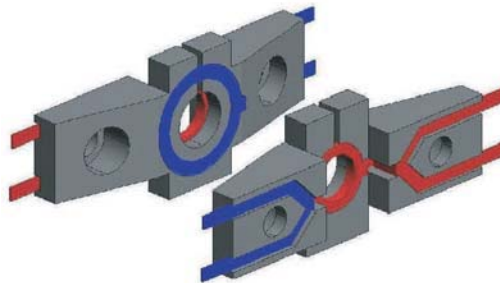


Figure 3.7: The faceplates, including incorporation of curvature coils (red) and anti-bias coils (blue).

The faceplate serves two main purposes: to hold the coils in their proper locations and to conduct away the heat generated by the coils during operation. The faceplates were constructed out of aluminum and subsequently anodized to themselves to prevent electrical shorts to the edges of the coils. The channels on the back of the faceplate allowed the current lead attachments to be made far from the coils themselves, as well as maintaining good thermal contact with the cold mount along their extent. The vertical

slice at the top of the faceplate prevented eddy currents from developing about the central aperture (which ultimately surrounded the cavity mirrors). The coils were inserted into place, with liberal amounts of silver epoxy, and again baked at 150°C to set the adhesive. This entire process was the most delicate of the entire assembly because of the relative violence inflicted upon the coils to get them properly inserted into the faceplates. The coil leads are under severe stress throughout assembly, and the extruding leads must endure one final violent procedure. In order to make a clean electrical connection to the coils with no contact resistance, the anodized layer of the extruding coil must be scraped off. If the leads break at any point then the coil must be removed and the faceplate scraped clean before attempting to insert another coil.

Further, the inserted coils must pass electrical tests showing that they are fully operational. A resistance drop of  $\sim 15 - 20\%$  (compared to the unwound aluminum strip) would imply a full shorting of one of the coil's turns. Any coil with a  $> 5\%$  resistance drop was deemed unacceptable. The coil must also be electrically isolated from the faceplate, and any perceived electrical contact also disqualified the coil and necessitated removal. After successful insertion of both curvature and anti-bias coils, the completed faceplate was again cleaned for UHV and awaited integration with the rest of the mount.

### 3.2.2 Gradient Coil Construction

Compared to the curvature and anti-bias coil construction, the gradient coils were far more robust. The aluminum strips used were 0.010" thick, and less prone to snapping. The coils consisted of 9 turns of wire, and the winding procedure was similar to that of the curvature and anti-bias coils.

Unlike the curvature/anti-bias coil assemblies, which are held in place by silver epoxy, the gradient coils were *not* epoxied throughout each layer but only on the edges which ultimately extrude from the trap mount. Mechanical pressure alone held the coils in place, as they were sandwiched between three mounting elements (described in the next subsection).

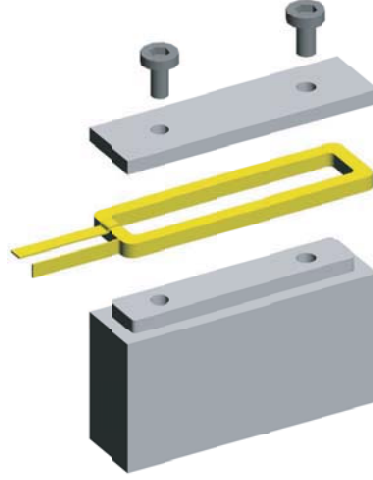


Figure 3.8: Diagram of gradient coil construction. Coil winding around the Teflon<sup>®</sup> mandrels is similar to Figure 3.4, though epoxy is only applied at the corners (see text).

### 3.2.3 Full Mount Assembly

The completed faceplates were affixed to anodized aluminum center pieces, constructed with center channels to allow future integration with the optical cavity. The same center pieces then had to allow the gradient coils to be incorporated into the assembly. The gradient coils were slid over the sides of the two center pieces, as shown in Figure 3.9. The picture of the central assembly also shows the current lead attachments on the sides of the center pieces. These elements were basically a custom copper lug structure which allowed electrical connection to the curvature and anti-bias leads without (a) electrical connection to the center mount or (b) any mechanical strain upon the coils when the assembly was integrated into the main chamber. The insulating material in this structure was Vespel<sup>®</sup>, a polyimide material which is easily machinable and acceptable for UHV conditions. The main RF antenna for millitrap evaporation is wound around the curvature/anti-bias attachment lugs after the electrical leads have been secured.

The assembly was finally completed as the center pieces and gradient coils were fixed into place by tightening (through clearance holes) the pieces between the main copper base and the top plates (both presented in Appendix D). A critical feature of the copper base

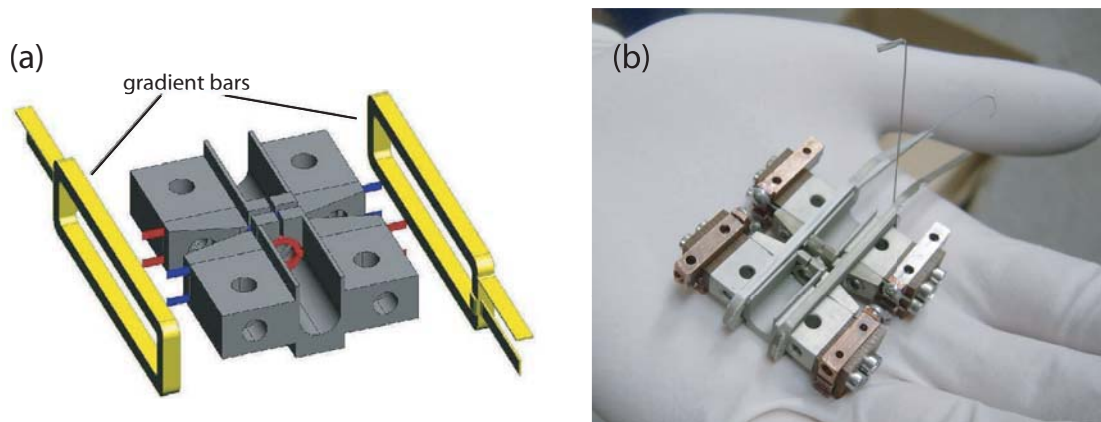


Figure 3.9: The Central Mount Assembly. (a) The faceplates are affixed to the center mount (see Appendix B) pieces, and the gradient bars are slid around the mount. (b) A photo of the assembled mount in the author’s hand. Note the extra structures on the side of the center piece; these are the attachment structure pieces for the curvature and anti-bias current leads.

was a closed channel for the heat exchanging liquid nitrogen flow, as shown in Figure 3.10.

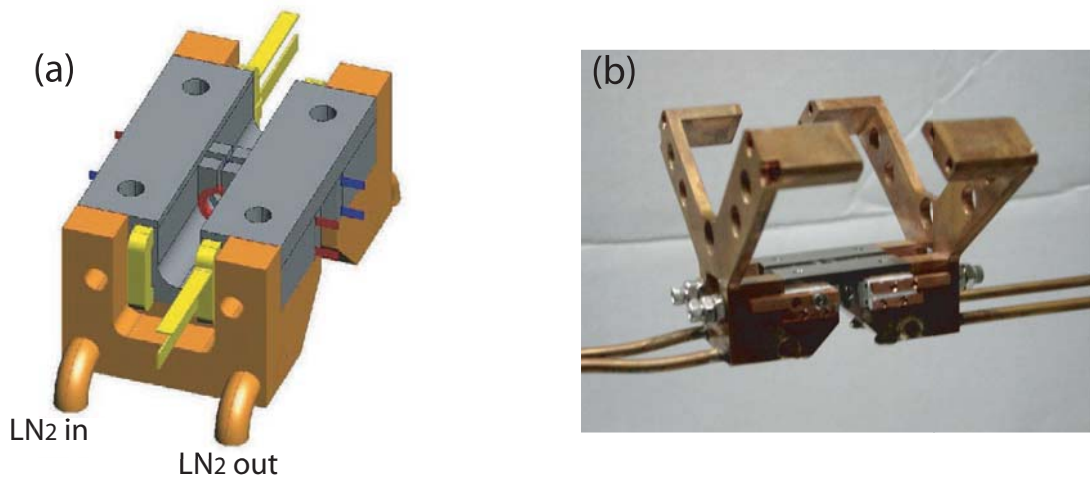


Figure 3.10: The full millitrap assembly. (a) The copper mount, with closed liquid nitrogen lines shown, is the final piece into which the millitrap is secured. Not shown are the winged structure which allows the copper mount itself to be affixed to the vacuum chamber. (b) A photo of the full millitrap assembly, with the mounting wings clearly seen.

Not shown in the diagram in Figure 3.10(a) are the “wings” which allow the mount

to be attached to the chamber, as well as accept the optical cavity assembly (described in chapter 6). A photograph of the actual assembly is shown in Figure 3.10(b).

### 3.2.4 Integration of the Millitrap with the Main Chamber

The winged assembly in Figure 3.10(b) is designed to mate with the mounting brackets which are seen on the inner edges of the 8" chamber in Figure 2.1. The copper wings are slightly thermally insulated by the use of Macor<sup>®</sup> spacers, though the 4-40 stainless steel threaded stock which fastens the millitrap assembly into place on these brackets does compromise this thermal insulation.

Once the millitrap was fastened into the chamber it had to be connected to the liquid nitrogen cooling line. After our group's negative experience with in-vacuum liquid connectors [63], we chose to silver solder the fluid connections on the millitrap. This nerve-racking procedure necessitated the immense skill of the late Armando Baeza, who brought the oxy-acetelene torch down into the basement lab and made the solder connections within two inches of the millitrap while hovering precariously over the optical table. The results speak for themselves, however, as the fluid line has never exhibited any leaks despite the daily operation at an internal LN<sub>2</sub> pressures of 100's of psi.

After the fluid solder joints were completed and the system passed the leak test, the twelve electrical connections were made. The intra-vacuum current carriers were 10AWG (0.102 in. OD) Kapton<sup>®</sup>-coated round copper wires. This heavy gauge was necessary because these wires carried in excess of 10 Amps in vacuum with no heat sinking between the vacuum feedthrough and the millitrap. With twelve thick wires and two  $\frac{1}{8}$ " copper tubes snaking through the same 2.75" opening and a small vacuum chamber, it was a non-trivial task to position the system where neither the MOT nor imaging optical paths were obscured. A picture of the vacuum chamber, millitrap, and connections is shown in Figure 3.11.

## 3.3 Operation of Millitrap

As should be evident from the involved manufacturing procedure, the millitrap was incredibly delicate and, once installed, a one-of-a-kind device. This fact was not lost

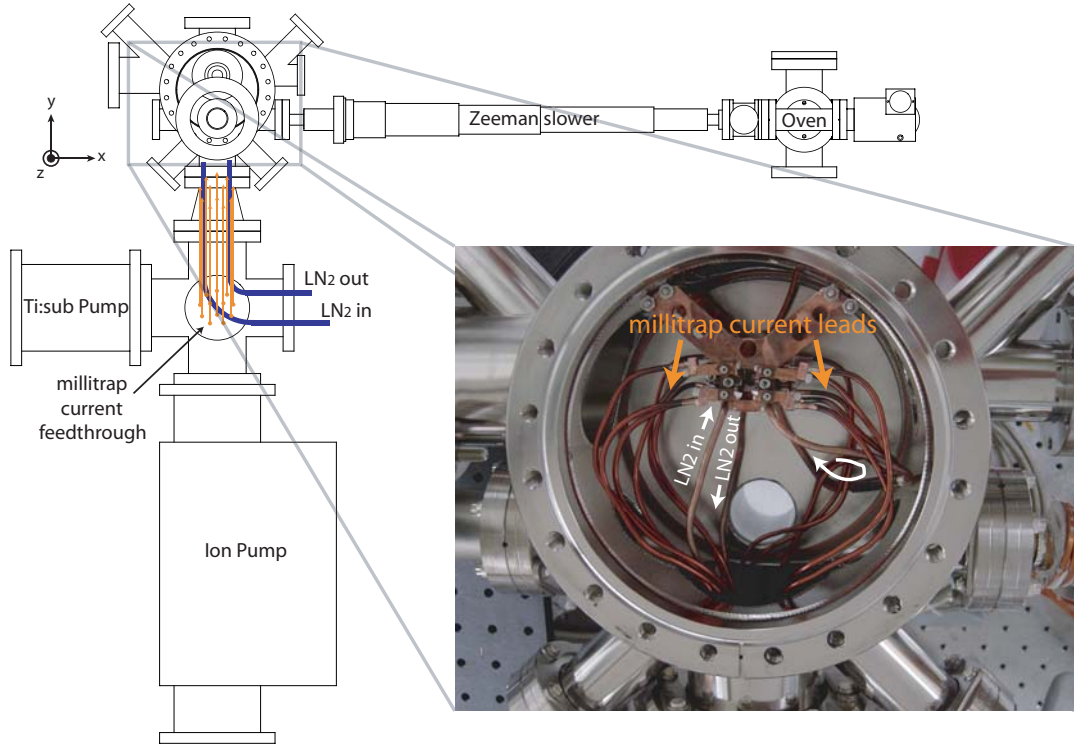


Figure 3.11: The millitrapping integration into the vacuum system. The drawing shows how the current and liquid nitrogen are delivered into the vacuum chamber, and finally to the millitrapping. The photo shows the central chamber assembly, with the twelve millitrapping current leads attached to the millitrapping, itself affixed to the interior chamber via the brackets seen in Figure 2.1. The closed-loop liquid nitrogen flow enters one half of the copper mount, out and into the second half, and finally out on the return line to be expelled from the vacuum chamber. (The output flow was actually then recycled into the Ti:sub shroud, which is not represented in this sketch.) The various leads shown must avoid obscuring optical access to the MOT region and the imaging axis of the millitrapping, giving the “spaghetti” appearance. While admittedly inelegant, these wires were also employed as anchors for the RF antennae used for quadrupole trap evaporation (not shown).

on its operators, and great care was taken to protect the millitrapping from any possible operational damage. The strain-relieved electrical connections all but guaranteed that the millitrapping could not be damaged in the vacuum wiring process, though it did periodically develop electrical shorts when closing the chamber due to compression and contact of the current delivery wires. Our greatest concern was the overheating and subsequent damage of the millimeter trap from excessive Joule heating. To prevent this, Tom Purdy

constructed an interlock system utilizing a Keithley Digital Integra Series 2701 Multimeter Data Acquisition System. With connections at the input measuring the voltage across and current through each coil, the Keithley measurement cycle monitored each of these twelve channels at least once per second. If any of the coil voltages or currents exceeded the prescribed set points, as would occur if the coils were heating up, then the interlock would trip and the electrical circuits were switched open. This system completely disallowed any room temperature operation of the trap above  $\sim 2$  Amps, and ensured that the millitrap coils would survive any liquid nitrogen flow interruption or accidental operation errors.

To provide the most flexibility in operating the millitrap, separate electrically-floating power supplies were used for each coil. Also included in the electrical setup were a set of CLC inductor-capacitor filters, though the values for the filters depended on the desired operation of the trap (DC traps vs. AC traps). Electrical characterization of the millitrap following the vacuum bakeout revealed several undesired low-resistance (several Ohm) connections between different coils, indicating electrical connections through the common mounting structure. These inter-coil connections should have no effect since independent supplies are used for each coil. The possible presence of undesired intra-coil connections, e.g. connections between turns on the multiple-turn coils, was tested by measuring parameters of magnetic traps formed with varying currents in each of the curvature, anti-bias, and gradient coils. No clear evidence for such flaws was obtained.

At least 150 psi of input pressure on the liquid nitrogen line was required to operate the trap at normal experimental currents. During this operation, Table 3.3 summarizes the observed performance of the coils (as well as the relevant dimensions). Following a bakeout of the millitrap at a temperature of  $250^{\circ}\text{C}$ , lifetimes of over 100 s were ultimately observed for atoms trapped in the millitrap, definitively demonstrating the vacuum compatibility of all materials used in its construction.

### 3.4 Atom Delivery to Millitrap

In the subsequent Section, we explore the possible millitrap field configurations, but the atom delivery to these trapping potentials remains nearly identical for all of the exper-

Coil	I.D.	O.D.	Thickness	Width	Cross-sec.	No. turns	$\dot{Q}$ @ 10 A
curvature	3 mm	4 mm	0.006 in.	1 mm	0.5 mm <sup>2</sup>	5	2 Watts
anti-bias	6 mm	8 mm	0.008 in.	0.75 mm	0.75 mm <sup>2</sup>	4	2 Watts
gradient	N/A	N/A	0.008 in.	2 mm	4 mm <sup>2</sup>	9	10 Watts

Table 3.1: Parameters for aluminum coil windings.

iments described in this thesis. As outlined in Section 2.5, approximately  $5 \times 10^9$  atoms are collected in the MOT, and subsequently  $2 \times 10^9$  atoms (in the  $|F = 1, m_F = -1\rangle$  manifold) are trapped in a spherical quadrupole trap. The magnetically-trapped atoms are transported 1.75" toward the millitrap. At this position both external quadrupole coils are running full current (see Table 2.5.2, forming a quadrupolar field  $\vec{B} = \{(104 \text{ G/cm})x, (158 \text{ G/cm})y, -(262 \text{ G/cm})z\}$ ). The atoms are then cooled via forced RF evaporation to 15  $\mu\text{K}$ , reducing the size of the cloud to 400  $\mu\text{m}$ , before transporting them the remaining distance to the center of the millitrap. This pre-cooling is crucial because the anti-bias coils in the IP trap allow only a 1 mm gap through which the atoms are threaded. A diagram of this process, including the size and phase space density of the cloud, is presented in Figure 3.12.

### 3.5 Spectrum of Millitrap Magnetic Trapping Potentials

The versatility of the millitrap is evidenced by the large number of trapping configurations it is capable of producing. This section presents a subset of these more traditional magnetic trapping configurations, and the subsequent chapter discusses an entirely different kind of magnetic trapping potential produced by the millitrap.

#### 3.5.1 Spherical Quadrupole Trap

Two coaxial circular coils, running current in the anti-Helmholtz configuration, will always produce a field zero somewhere along their common z-axis. Because there are four coaxial coils in the millitrap, this opens up three possible spherical quadrupole implementations: curvature/curvature, anti-bias/anti-bias, and curvature/anti-bias. Utilizing

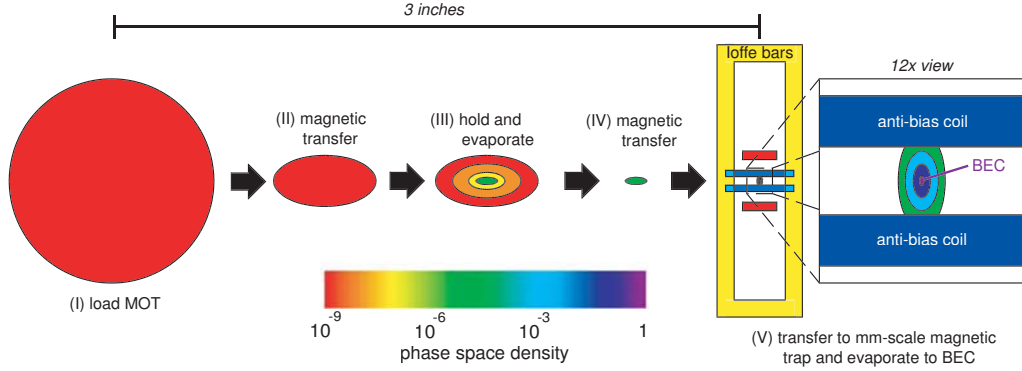


Figure 3.12: Sketch of experimental sequence for BEC in the millitrap (Ioffe-Pritchard configuration). (I) Atoms are loaded into the MOT and subsequently trapped in a spherical quadrupole trap. (II) The atoms are then transferred 1.75 inches towards the mm-scale IP trap and (III) evaporated to a phase space density of  $\Gamma \sim 10^{-5}$ . (IV) The cloud is magnetically transferred into the IP trap and (V) captured by a curvature coil and an anti-bias coil in a spherical quadrupole trap. The full millitrap is then turned on and the atoms are confined in the IP field with a 2 G bias field. The cloud is then further evaporated, forming a pure BEC of 1 million atoms.

the curvature/anti-bias quadrupole trap is advantageous if an Ioffe-Pritchard trap will be employed later in the experimental sequence, as the coil currents will already be running in the correct directions for this configuration. The curvature/curvature spherical quadrupole boasts the highest gradient/current ratio at 13.8 G/cm/A, but suffers from large off-axis inhomogeneities due to the geometry of the coils. The anti-bias/anti-bias spherical quadrupole is the “best” spherical quadrupole in that it can be displaced over a large distance with a transverse bias field with minimal distortion of the trap; its gradient/current ratio is 6.6 G/cm/A. This advantageous feature makes possible the delivery of Bose-condensed atoms to the high-finesse optical cavity (as presented in chapter 6), and is also the basis for the Time-Orbiting Potential trap presented later in this section.

### 3.5.2 Ioffe-Pritchard Trap

The Ioffe-Pritchard (IP) trap is the magnetic field configuration for which the millitrap was designed, and a number of results from our initial investigations were published in Ref. [54]. Some the main results include (a) the demonstration of  $N > 10^6$  atom BECs in an IP field with the expected large curvatures ( $B_z'' = 7800 \text{ G/cm}^2$  at 10.5 Amps), (b) the

associated wide spectrum of trapping geometries with control of the transverse trapping frequencies, and (c) a wide range of tilt angles with respect to the z-axis.

One unexpected feature of this strong IP trap was a remarkably high efficiency of RF evaporation. This efficiency can be quantified by comparing the factor gained in phase space density  $\Gamma$  through the evaporative cooling loss of a given factor in atom number  $N$ , obtaining, e.g. a figure of merit  $f = -d \ln \Gamma / d \ln N$ , with  $\Gamma$  and  $N$  parameterized along some evaporation trajectory. Typical figures of merit cited in the literature for evaporation from IP traps are  $f = 2$  to  $f = 3$  [80, 81]. In our mm-scale IP trap, a factor of over  $10^5$  in phase space density is efficiently gained by evaporative cooling to the Bose-Einstein condensation transition temperature with an overall figure of merit of  $f = 4.5$ . The distinct advantage of this large figure-of-merit is seen in Figure 3.13, where BEC transition is reached with an order of magnitude higher atom number than would have been achieved in typical traps.

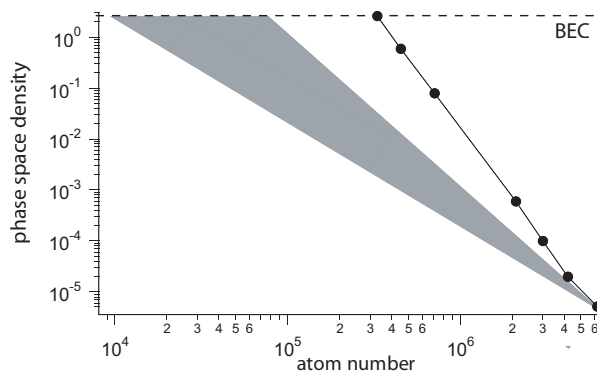


Figure 3.13: Typical phase space trajectory in the millitrap (Ioffe-Pritchard configuration). Shown for reference in grey is the domain of more typical magnetic trapping implementations (see text).

To account for this high efficiency, we note that the IP trap, aside from being strongly confining and thus compressing atomic clouds to high collision rates, is also nearly isotropic. We suspect that the condition of near isotropy improves the efficiency of evaporative cooling relative to that in the typically-used anisotropic traps since high-energy atoms produced collisionally in the gas can easily escape the center of the cloud in *any direction*, and thereby reach the trap boundary established by the applied RF radiation. In contrast, in a cigar-shaped cloud with high aspect ratio, the large axial collisional depth can prevent

the escape of all high-energy atoms except those traveling nearly purely in the radial direction. Further, we note that high evaporation efficiency is obtained in our trap in spite of the vertical orientation of the axial direction. In contrast, IP traps with weaker axial confinement are rarely oriented in this manner so as to avoid the onset of lower dimensional evaporation due to gravitational sag [81, 82].

### 3.5.3 Time-Orbiting Potential Trap

While the Ioffe-Pritchard trap is operated with steady DC currents in its constituent coils, the first experimental observation of dilute gas BEC [83] occurred in an AC trap known as a Time-Orbiting Potential (TOP) trap [20, 84]. For our system, a spherical quadrupole trap is produced by the anti-bias coil pair and biased by a *rotating* field of  $\mathbf{B}_r = B_r (0, \cos \omega_r t, \sin \omega_r t)$ . The rotating field is produced by the curvature coils and the gradient coils, both running current in the Helmholtz configuration. The resultant field is given by

$$\mathbf{B} = (B'x, B'y + B_r \cos \omega_r t, -2B'z + B_r \sin \omega_r t) . \quad (3.8)$$

If  $\omega_r$  is much greater than the motional timescales of the atoms, then taking the time-average of the field is appropriate. We are also concerned with regions about the origin, which makes the product  $|B'r/B_r| \ll 1$ . To find the time-averaged field, we look to the magnitude of  $\mathbf{B}$  to lowest order in  $|B'r/B_r|$ :

$$\begin{aligned} \langle |\mathbf{B}| \rangle_t &= \langle \sqrt{B'^2 x^2 + (B'y + B_r \cos \omega_r t)^2 + (-2B'z + B_r \sin \omega_r t)^2} \rangle_t \\ &\approx B_r + \frac{B'^2}{4B_r} (2x^2 + y^2 + 4z^2) . \end{aligned} \quad (3.9)$$

This harmonic trap has a  $\sqrt{2} : 1 : 2$  aspect ratio<sup>7</sup>.

To produce a TOP trap in the millitrap, we had to rewire the coils such that a quadrupole field was produced by the anti-bias coils (operating in anti-Helmholtz configuration) and the orbiting fields described above enacted by the gradient coils and curvature coils (both operating in an Helmholtz configuration). The atoms were brought into the millitrap region and transferred to an anti-bias/anti-bias quadrupole trap, formed 1 mm from

<sup>7</sup>In contrast, an orbiting field in the transverse plane has a  $1 : 1 : 2\sqrt{2}$  aspect ratio.

the center axis<sup>8</sup>. Typical operating conditions for the millitrap-produced TOP field were  $B' = 36$  G/cm, with an orbiting frequency of  $\omega_r = 2\pi \times 5$  kHz loaded at  $B_r = 8.6$  G. After initial “circle of death” evaporation in this trap, the orbiting field was lowered to the final value of  $B_r = 6.3$  G, where the trapping frequencies were  $(\omega_x, \omega_y, \omega_z) = 2\pi \times (72, 51, 102)$  Hz. Here the cloud underwent forced RF evaporation to quantum degeneracy, and nearly pure BECs of  $> 40,000$  atoms were observed.

---

<sup>8</sup>This off-axis move is made to avoid the cavity which, at the time we implemented this trap, was obscuring the center axis. To form this trap outside the cavity center a transverse bias field along the  $y$ -axis is applied, provided by wires wrapped around the 4.5” “cavity structure” flange in Figure 2.1, forming a “push coil” capable of displacing the  $B' = 36$  G/cm quadrupole trap many millimeters.